
SonoGym: High Performance Simulation for Challenging Surgical Tasks with Robotic Ultrasound

Yunke Ao
Balgrist University Hospital
ETH Zurich

Masoud Moghani *
University of Toronto
NVIDIA

Mayank Mittal *
ETH Zurich
NVIDIA

Manish Prajapat
ETH AI Center
ETH Zurich

Luohong Wu
Balgrist University Hospital
University of Zurich

Frederic Giraud
Balgrist University Hospital
University of Zurich

Fabio Carrillo
Balgrist University Hospital
University of Zurich

Andreas Krause
ETH AI Center
ETH Zurich

Philipp Fürnstahl
Balgrist University Hospital
University of Zurich

Abstract

Ultrasound (US) is a widely used medical imaging modality due to its real-time capabilities, non-invasive nature, and cost-effectiveness. Robotic ultrasound can further enhance its utility by reducing operator dependence and improving access to complex anatomical regions. For this, while deep reinforcement learning (DRL) and imitation learning (IL) have shown potential for autonomous navigation, their use in complex surgical tasks such as anatomy reconstruction and surgical guidance remains limited — largely due to the lack of realistic and efficient simulation environments tailored to these tasks. We introduce SonoGym, a scalable simulation platform for complex robotic ultrasound tasks that enables parallel simulation across tens to hundreds of environments. Our framework supports realistic and real-time simulation of US data from CT-derived 3D models of the anatomy through both a physics-based and a generative modeling approach. Sonogym enables the training of DRL and recent IL agents (vision transformers and diffusion policies) for relevant tasks in robotic orthopedic surgery by integrating common robotic platforms and orthopedic end effectors. We further incorporate submodular DRL—a recent method that handles history-dependent rewards—for anatomy reconstruction and safe reinforcement learning for surgery. Our results demonstrate successful policy learning across a range of scenarios, while also highlighting the limitations of current methods in clinically relevant environments. We believe our simulation can facilitate research in robot learning approaches for such challenging robotic surgery applications. Dataset, codes, and videos are publicly available at <https://sonogym.github.io/>.

1 Introduction

Ultrasound is a commonly used medical imaging technique because it is non-invasive, cost-effective, and capable of providing real-time images [16]. While freehand ultrasound is operator-dependent and skill-intensive, *robotic ultrasound* systems have been developed to enhance reproducibility and

*Equal second author contribution. Correspondance to: yunke.ao@balgrist.ch

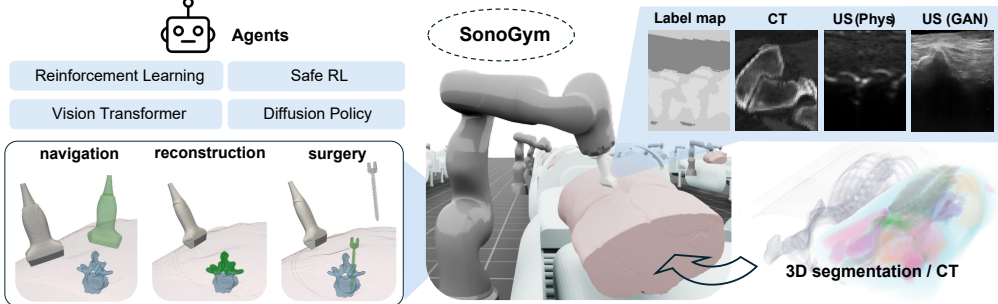


Figure 1: Overview. SonoGym provides model-based and learning-based ultrasound (US) simulation using 3D label map and CT scans from real patient datasets. Tasks in SonoGym include US navigation, anatomy reconstruction, and US-guided robotic surgery. SonoGym enables benchmarking of various algorithms, including reinforcement learning (RL), safe RL, vision transformer, and diffusion policy.

improve imaging efficiency [17]. Additionally, due to its ability to penetrate soft tissues, robotic ultrasound has been used for intraoperative guidance in various surgical procedures [36].

Robotic ultrasound has been particularly impactful and widely adopted in orthopedic surgery, which often has limited visibility and high precision requirements. These applications can be categorized into three main tasks: *navigation*, *anatomy reconstruction*, and *ultrasound-guided surgery*. For *navigation*, the ultrasound probe can be manipulated autonomously to localize and track target anatomy [51, 5]. For *anatomy reconstruction*, robotic ultrasound has been used to scan and reconstruct the dorsal surface of the spine, which can then be registered with preoperative CT images to guide surgical steps [24, 49]. While these systems employ *heuristic* path planning for the ultrasound probe, determining an *optimal* scanning path based solely on ultrasound image feedback remains a challenging open problem. Complete robotic ultrasound-guided spinal *surgery* pipelines have also been developed [22, 25], but they often rely on registration between ultrasound and preoperative CT images, lacking more intelligent planning directly informed by ultrasound image inputs.

Deep Reinforcement Learning (DRL) and Imitation Learning (IL) have shown strong potential in addressing such complex vision-based decision-making problems [18, 30, 6, 56]. Numerous studies have applied DRL and IL to autonomous robotic ultrasound *navigation* [12, 34, 23]. However, their use in ultrasound-guided *reconstruction* and orthopedic *surgery* remains largely unexplored.

One key limitation to the broader use of DRL and IL in robotic ultrasound is the absence of high-performance, realistic simulation environments. In other areas of robotics, simulation-based DRL training has proven highly effective [30, 1, 14, 47], supported by platforms such as NVIDIA IsaacLab [31], IsaacGym [28], PyBullet [7], and Mujoco [48]. In this work, our objective is to develop a comprehensive, efficient robotic ultrasound simulation platform that enables simulating not only *navigation*, but also other challenging tasks covered by ultrasound-guided surgical procedures, such as *reconstruction* and execution of *surgery*.

Our main contributions are summarized as follows: (i) We present a realistic and efficient robotic ultrasound simulation platform, SonoGym, which includes multiple anatomical models of the real patient from TotalSegmentator [52] and supports both model-based and learning-based ultrasound simulation, as shown in Fig.1. (ii) We formulate ultrasound-guided navigation, reconstruction, and surgery as specialized Markov Decision Processes (MDPs), enabling the training of high-performing DRL agents. To more effectively capture task-specific challenges, we adapt these models to partially observable MDPs (POMDPs), submodular MDPs [37], and state-wise constrained MDPs [57]. (iii) We generate expert demonstration datasets within our simulator to enable training of recent IL agents, including the Action Chunking Transformer (ACT, [56]) and the Diffusion Policy (DP, [6]). (iv) We conduct extensive evaluations and comparisons of DRL and IL approaches across the different tasks, analyzing their generalization performance across different ultrasound noise and different patient models; These results help assess the potential of DRL and IL and the challenges that remain in this application domain.

2 Related Works

Simulation platforms for robotic surgery. Multiple simulation platforms have been developed to support DRL training for various surgical tasks. LapGym [39] provides a simulation environment for robot-assisted laparoscopic surgery with soft-tissue deformation based on the SOFA framework [10]. SurRol [54, 27] enables surgical robot learning compatible with the da Vinci Research Kit [20], based on PyBullet. Surgical Gym [40] allows the training of various surgical robotic arms to reach desired positions. Orbit-surgical [33, 55] provides various surgical manipulation environments with photorealistic rendering, enabling the training of visuomotor (from vision to action) policies using DRL or IL. So far, most existing surgical simulation platforms focus on laparoscopic (minimally invasive) surgery or soft tissue manipulation, with few providing realistic patient models like [33] and intraoperative medical imaging modalities such as ultrasound.

Efficient ultrasound simulation. Real-time and realistic ultrasound simulation has been a long-standing research topic. Traditional approaches employ GPU-accelerated ray tracing based on CT images or segmentation maps [21, 38, 43, 4, 9, 29]. We adopt a model-based simulation approach based on [38, 21] in our framework. Recently, generative networks have also been leveraged for ultrasound image simulation, enabling more realistic image patterns while maintaining fast inference. For example, Liang *et al.* [26] and Alsinan *et al.* [2] explored the generation of ultrasound images based on composite label maps or bone sketches using Generative Adversarial Networks (GAN, [11]). Song *et al.* [45] studied learning-based CT-to-ultrasound translation with CycleGAN [58]. However, these approaches have not been utilized for training DRL or IL agents. Although diverse and realistic ultrasound images can also be generated using diffusion models [46, 8, 19], we adopt a GAN-based approach [15] to maintain simulation efficiency. With a high-quality in-house paired CT-ultrasound dataset [53], we can train effective GANs tailored for orthopedic surgery.

Simulation and robot learning for robotic ultrasound. DRL or IL-based robotic ultrasound navigation has been widely explored. However, many existing works utilize their own ultrasound sweep dataset or simulation. For instance, Hase *et al.* [12] and Li *et al.* [23] applied deep Q-learning on in-house collected ultrasound sweeps to learn a navigation policy for the spine. Ning *et al.* [34] develop a robotic ultrasound environment to train a policy for ultrasound image acquisition based on RGB image observation, therefore, their simulation only involves the RGB camera, robot and soft tissues, without incorporating an ultrasound simulation. Ao *et al.* [3] investigate intraoperative surgical planning based on reconstructed bone surface from ultrasound, but they only simulate noisy bone surface reconstructions without raw ultrasound images. In contrast to them, our work further provides realistic ultrasound image simulation for orthopedic surgery and relevant anatomy, along with incorporating challenging tasks such as ultrasound-guided *surgery* and bone surface *reconstruction*.

3 Preliminaries

3.1 Reinforcement learning

Markov decision process. An MDP is a tuple of $\langle \mathcal{S}, \mathcal{A}, \mathcal{P}, \rho, \mathcal{O}, T, \mathcal{R} \rangle$, where \mathcal{S} is the state space with state $s \in \mathcal{S}$, \mathcal{A} is the action space with action $a \in \mathcal{A}$, \mathcal{P} is the transition probability, ρ is the initial state distribution, \mathcal{O} is the observation space with observation $o \in \mathcal{O}$, and \mathcal{R} is the reward space with $r \in \mathcal{R}$. An episode starts at $s_0 \sim \rho$, and at each time step $t \geq 0$ at state s_t , the agent receives an observation o_t and it draws an action a_t conditioned on it according to a policy $\pi : \mathcal{O} \times \mathcal{A} \rightarrow [0, 1]$. Applying this action, the simulation environment evolves to a new state s_{t+1} following the MDP transition \mathcal{P} and receives a reward $r(s, a)$. For the typical RL task described above, we deploy the proximal policy optimization (PPO, [41]) and Advantage Actor Critic (A2C, [32]) algorithms.

State-wise constrained MDP. The MDP is appended with the cost functions $C_i : \mathcal{S} \times \mathcal{A} \rightarrow \mathbb{R}, \forall i \in [m]$ with a total of m constraints [57]. The feasible policy class Π_c for this MDP satisfies $\mathbb{E}[C_i(s_t, a_t)] \leq w_i, \forall i \in [m]$ and $\forall t \in [T]$ where w_i are constraint thresholds. For the state-wise constrained RL problem, we implement a modified version of SafeRPlan [3], in which the safety distance prediction network is adapted to predict the cost $\hat{C}_i(s_t, a_t)$ instead of the distance. During testing, no action is taken if any cost prediction exceeds a threshold, *i.e.*, $\hat{C}_i(s_t, a_t) > w_i - \delta$, where δ is a margin that adjusts the level of conservatism.

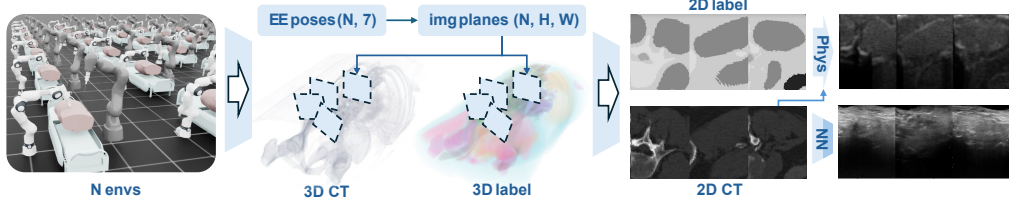


Figure 2: Efficient ultrasound simulation across a large number of environments. Given the current end-effector poses of the robot arms, we first compute the ultrasound image planes in the patient frames attached with 3D CT volumes and label maps. We then extract 2D CT and label slices as pixels on the plane. Ultrasound images are subsequently simulated based on these inputs using either physics-based models or neural networks.

Submodular MDP. The MDP here is appended with non-additive trajectory-based rewards, in contrast to state rewards defined above. We replace \mathcal{R} with a set function $F : 2^{T \times S} \rightarrow \mathbb{R}$, which is a monotone submodular function (*c.f.* [37]). We denote the trajectory with τ and for each (partial) trajectory $\tau_{l:l'}$, we use the notation $F(\tau_{l:l'})$ to refer to the objective F evaluated on the set of (state, time)-pairs visited by $\tau_{l:l'}$. Computationally, solving the submodular MDP problem is intractable; however as proposed in [37], we use a PPO variant of submodular policy optimization, *i.e.*, use marginal gain as reward at state $r(s_t, a_t) = F(s_{t+1}|\tau_{0:t}) := F(\tau_{0:t+1}) - F(\tau_{0:t})$. This results in greedy maximization of rewards at each step, which is empirically shown to perform well [37].

3.2 Imitation Learning

Action chunking transformer [56]. In ACT, a policy is learned to predict a sequence of actions (action chunk) given the current observation $\pi(a_{t:t+k}|o_t)$, where k is the sequence length. To address the noise from the expert data, the policy is trained as a conditional variational autoencoder (CVAE, [44]), using Transformer architectures [50]. During inference, the policy predict an action chunk at each time step, and the final action is smoothed using a *temporal ensemble* (averaging predictions from different previous steps).

Diffusion policy (DP) [6]. In DP, a visuomotor policy $\pi_\theta(a_{t:t+k}|o_{t-h:t})$ is trained using Denoising Diffusion Probabilistic Models (DDPM, [13]) to predict a sequence of actions $A_t := a_{t:t+k}$ given the historical visual observation input $O_t := o_{t-h:t}$, where k is the horizon length, h is the number of steps for the latest observations. Then DDPM performs M denoising steps to generate $A_t^{M-1}, A_t^{M-2}, \dots, A_t^0$ based on a noise prediction network $\epsilon_\theta(O_t, A_t^m, m)$:

$$A_t^{m-1} = \alpha(A_t^m - \gamma\epsilon_\theta(O_t, A_t^m, m) + \eta_m), \quad m = M, M-1, \dots, 1, \quad \eta_m \sim \mathcal{N}(0, \sigma^2 I),$$

where α, γ, σ are determined by the noise scheduler. ϵ_θ is trained using pairs of Gaussian noise η_m and ground truth actions \bar{A}_t^0 by minimizing loss $\|\eta_m - \epsilon_\theta(O_t, \bar{A}_t^0 + \beta_m \eta_m, m)\|^2$, where β_m depends on the noise scheduler.

4 SonoGym Environments

We discuss the three robotic ultrasound-guided tasks: *navigation*, bone surface *reconstruction*, and spinal *surgery*, supported by our SonoGym platform with realistic ultrasound simulations, as is shown in Fig.1. In the following, we introduce the components and tasks of SonoGym in detail.

Assets. We describe the main components of our simulation environments: robot arms, patient models, and end effectors (surgical drills and ultrasound probes). We support multiple robotic arm models, including KUKA Med14 and Franka Emika Panda, both of which can be equipped with either an ultrasound probe or a drill at the end effector. The robot arm simulation and its corresponding inverse kinematic controllers are adopted from NVIDIA IsaacLab. We provide patient models derived from the TotalSegmentator dataset [52], which include 3D anatomical segmentations and corresponding CT images. For each patient in a subset of the dataset, we generate target trajectories on the L4 vertebra to guide robotic drilling, which serves as the objective for the *surgery* task.

Ultrasound simulation. We explain the pipeline to simulate ultrasound images based on patient-specific 3D CT scans and segmentation maps, as shown in Fig.2. We first compute the ultrasound image planes in the patient coordinate frames, using the end-effector poses of the robot arm. We then extract the corresponding pixels on the image planes from the 3D CT volume and segmentation map to generate 2D CT and label slices. For model-based (MB) simulation, we adopt the convolution-based method from [38] to simulate ultrasound images from the label slice, and refine the reflection term using the CT slice similar to [21]. For learning-based (LB) simulation, we train a generative model using the pix2pix framework [15] to translate CT slices into ultrasound images, leveraging a large in-house CT-to-ultrasound paired dataset collected from 7 ex-vivo spine specimens [53]. We apply intensity histogram matching between the input CT slices and a subset of training CT images to mitigate the domain gap in learning-based simulation. Both learning-based and model-based simulations are executed in batch mode across parallel environments to maintain computational efficiency.

4.1 Task 1: Ultrasound navigation

Task description. We consider the problem of navigating an ultrasound probe to locate a target anatomy, starting from a random initial position on the back of the patient. The target pose of the ultrasound probe with frame $\{U\}$ is represented by a fixed goal frame $\{G\}$ located above the target anatomy, shown in orange in Fig.3 (left). In practice, the precise frame of the target anatomy $\{G\}$ is typically *unknown* in a real patient. However, the real-time ultrasound image partially visualizes the underlying anatomy and implicitly encodes the position of the probe ($\{U\}$) relative to the goal frame ($\{G\}$), which can be exploited for navigation. To ensure continuous image acquisition, the ultrasound probe must maintain stable contact with the skin. We assume this contact is maintained by an existing low-level robot controller, which also enforces the probe to remain perpendicular to the skin surface (*i.e.*, the z -axis of the probe aligns with the local surface normal). Our focus is solely on task-space planning of the *3 DoF tangential motion* of the ultrasound probe along the skin surface to reach the goal frame.

States and observations. At any time t , the state $s_t \in \mathcal{S} \subseteq \mathbb{R}^6$ consists of the relative position ${}^G_U p_t \in \mathbb{R}^3$ and angle-axis orientation ${}^G_U q_t \in \mathbb{R}^3$ between the ultrasound probe frame U and the goal frame G . The observation is the real-time ultrasound image feedback $o_t \in \mathcal{O} \subseteq \mathbb{R}^{H \times W}$, where H, W denote the height and width of the images, respectively.

Actions and reward. The action is defined over the remaining degrees of freedom in the ultrasound probe frame U as $a_t := [\Delta x_t, \Delta y_t, \Delta \alpha_t]^\top \in \mathbb{R}^3$, where $[\Delta x_t, \Delta y_t]^\top$ represents horizontal translations on the skin surface (along the x and y axes of U , shown green in Fig. 3 (left)), and $\Delta \alpha_t$ denotes rotation around the surface normal (z axis of $\{U\}$). The reward is defined as the change in distance to the goal frame: $r_t = w_1(\|{}^G_U p_t\| - \|{}^G_U p_{t+1}\|) + \|{}^G_U q_t\| - \|{}^G_U q_{t+1}\|$, where w_1 is a tunable weight.

Agents. We support training PPO agents, which achieve high performance for navigation. For the network architecture, we use a shared convolutional neural network (CNN) encoder for the policy and value networks. Furthermore, we provide datasets for the training of imitation learning agents (such as ACT and DP), which are collected with an *expert policy* based on the true state ${}^G_U p_t$ and ${}^G_U q_t$. The *expert policy* is defined as $a_t^* = \rho_1 [{}^G_U p_t \cdot e_x, {}^G_U p_t \cdot e_y, {}^G_U q_{t+1} \cdot e_z]^\top$, where $\rho_1 < 1$ is the proportional scaling parameter, e_x, e_y, e_z denotes the unit vectors along the x, y, z axes of $\{U\}$. We train ACT and DP with the default architecture described in [56, 6].

4.2 Task 2: Bone surface reconstruction

Task description. We consider the robotic ultrasound spine surface reconstruction problem following the setup in [24], and simplify the task to reconstruct only the surface of a single vertebra. We assume that the bone surface can be segmented from each 2D ultrasound image using segmentation methods such as [35]. The 3D reconstruction of the vertebra surface can be obtained by combining these segmentations across frames, together with the tracked pose of ultrasound probes. Our task focuses on optimal path planning of the ultrasound probe on the skin surface to enable fast and sufficient reconstruction for registration, as is shown in Fig. 3 (middle). Compared to the navigation task setting, we additionally allow adjustment of the pitch angle (rotation around the y -axis of the $\{U\}$ frame) to capture more surface points. This planning problem is challenging because the pose of the target

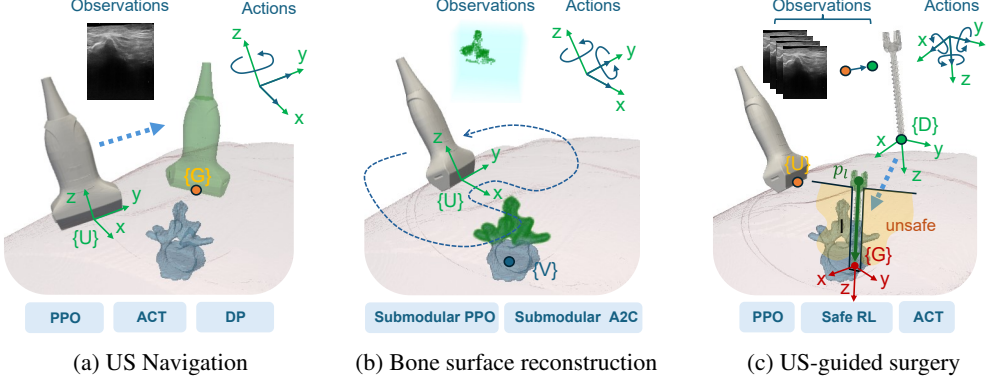


Figure 3: **Tasks.** The target anatomy (L4 vertebra) is colored dark blue. **(a) Ultrasound (US) navigation:** Move the ultrasound probe to the goal pose (green) based on the real-time ultrasound images. **(b) Bone surface reconstruction:** Efficiently scan the surface of the target vertebra (green) with a low path length. **(c) Ultrasound-guided spinal surgery:** Fix the ultrasound probe to track the target vertebra, and drill inside the vertebra safely based on the ultrasound image and tracked poses of the ultrasound probe and drill. Supported algorithms are illustrated below each task.

vertebra $\{V\}$ is unknown, requiring the planner to balance exploration and exploitation based on the current reconstruction.

State and observations. Our state s_t is the (unknown) position ${}^U_V p_t \in \mathbb{R}^3$ and angle-axis orientation ${}^U_V q_t \in \mathbb{R}^3$ of the ultrasound probe in the target vertebra frame $\{V\}$. The observation is defined as the current reconstruction $\mathcal{M}_{0:t}$ transformed to the current ultrasound frame ${}_U \mathcal{M}_{0:t}$ and voxelized to a 3D image of shape $H \times W \times E$, as is shown in Fig.3 (middle), where H, W, E denote the image height, width, and elevation, respectively. It partially encodes the current reconstruction status and the relative poses ${}^U_V p_t, {}^U_V q_t$.

Actions and reward. The 4D action is defined as $a_t := [\Delta x_t, \Delta y_t, \Delta \alpha_t, \Delta \beta_t]^\top$, corresponding to translation along x, y axes and rotation around z, y axes in $\{U\}$ frame. The trajectory objective function F accounts for both the total number of acquired surface points and the trajectory length, and is given by: $F(\tau_{0:t}) := |\mathcal{M}_{0:t}| - w_2 \sum_{h=0}^t (|\Delta x_h| + |\Delta y_h| + w_3 |\Delta \alpha_h| + w_3 |\Delta \beta_h|)$, where w_2, w_3 are tunable weights, $|\mathcal{M}_{0:t}|$ denotes the area of the surface $\mathcal{M}_{0:t}$.

Agents. We support training submodular PPO and A2C, which achieved strong performance in our task. Both policy and value function networks share a CNN encoder, with separate heads for actions and values. For comparison, we also provide heuristic open-loop path planning, following the approach described in [24].

4.3 Task3: Ultrasound-guided surgery

Task description. We consider the ultrasound-guided path planning problem in robotic bone drilling for pedicle screw placement. During surgery on a real patient, the exact position of the target vertebra to be drilled is not directly known. To localize the target vertebra, we assume a 3D ultrasound probe is navigated above the region of interest, as shown in Fig.3 (right), continuously acquiring volumetric ultrasound images $I_t \in \mathbb{R}^{H \times W \times E}$. The poses of both the ultrasound probe frame $\{U\}$ and the drill frame $\{D\}$ are tracked by the robotic tracking system. The objective is to safely and accurately drill into the vertebra by following a predefined path (green in Fig. 3 (right)), using the acquired ultrasound images and pose tracking. This path starts from a point p_l on the skin surface and leads to a target goal frame ($\{G\}$, red), which is defined by the surgeon directly on the vertebra.

States and observations. The state $s_t \in \mathcal{S} \subseteq \mathbb{R}^6$ consists of the relative position ${}^D_G p_t \in \mathbb{R}^3$ and angle-axis orientation ${}^D_G q_t \in \mathbb{R}^3$ between the goal frame $\{G\}$ and the current drill frame $\{D\}$. The observation o_t includes the volumetric ultrasound images I_t and the tracked relative pose between the ultrasound probe and the drill, $[{}^U p_t, {}^U q_t'] \in \mathbb{R}^7$, where ${}^U q_t'$ is a quaternion. To simulate noise in ultrasound-based navigation, we randomize the position of the ultrasound probe above the target vertebra by up to a user-specified threshold λ .

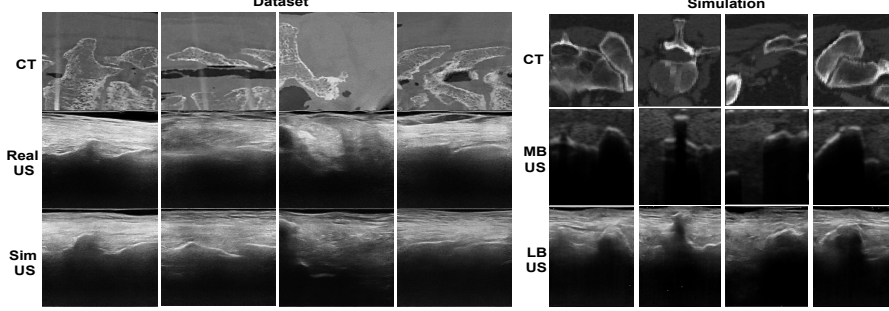


Figure 4: **Qualitative evaluation of ultrasound (US) simulation.** (left) Evaluation with the testing dataset. The top row shows 2D CT slices of the human specimen. The corresponding real US and the generated US of Sonogym are shown in the rows below. (right) Examples of simulated US images in SonoGym. Sliced CT, model-based (MB) US simulation, and learning-based US simulation are shown in the top, middle, and bottom rows, respectively. The learning-based US simulation has high visual similarity to real US images.

Actions, reward and cost. The action is defined as the 6D command for the drill in $\{D\}$ frame: $a_t := [{}_D\Delta p_t, {}_D\Delta q_t]$, where ${}_D\Delta p_t$ is the translation and ${}_D\Delta q_t$ is the rotation vector. While the drill can move freely outside the patient, it must remain within a narrow region once inside to ensure safety, as illustrated in Fig. 3 (right). To facilitate reward design, we define the free region $\mathcal{C}_{\text{free}}$ and drilling region $\mathcal{C}_{\text{drill}}$ in $\{G\}$ as follows:

$$\mathcal{C}_{\text{drill}} := \{p \mid \sqrt{p_x^2 + p_y^2} \leq \frac{d}{2}, -l \leq p_z \leq 0\}, \quad \mathcal{C}_{\text{free}} := \{p \mid p_z \leq -l\},$$

where p_x, p_y, p_z are the x, y, z components of the arbitrary position p , l is the distance from skin to the goal, d is the diameter of the drill region. The remaining space is defined as the unsafe region $\mathcal{C}_{\text{unsafe}}$. The reward is defined as

$$r_t := \begin{cases} w_4 (\|{}_G^D p_t - p_l\| - \|{}_G^D p_{t+1} - p_l\|) + w_5 (\|{}_G^D q_t\| - \|{}_G^D q_{t+1}\|), & \text{if } {}_G^D p_t \in \mathcal{C}_{\text{free}}, \\ w_6 (\|{}_G^D p_t\| - \|{}_G^D p_{t+1}\|) + w_5 (\|{}_G^D q_t\| - \|{}_G^D q_{t+1}\|), & \text{if } {}_G^D p_t \in \mathcal{C}_{\text{drill}}, \\ 0 & \text{otherwise.} \end{cases}$$

and 0 otherwise. Here $p_l := [0, 0, l]$ is the surface point directly above the goal, w_4, w_5, w_6 are tunable weights. This reward encourages agents to first reach the skin point p_l before beginning the drilling process. The cost for the state-wise constrained MDP is the indicator function of the unsafe region $c_t := \mathbb{I}[{}_G^D p_t \in \mathcal{C}_{\text{unsafe}}]$.

Agents. We provide both PPO and modified SafeRPlan agents for the task. A CNN and an MLP are used as encoders for the image and relative pose observations, respectively. We also provide datasets collected from an expert policy (with expert action a_t^*), which moves the drill towards the skin point p_l first, then towards $\{G\}$. We support the training of ACT using the collected dataset.

5 Experiments

In this section, we demonstrate the effectiveness of the proposed simulation environment by training and comparing the performance of RL and IL algorithms. In the experimental study, we are interested in answering the following four research questions. (1) How realistic and efficient is the ultrasound simulation? (2) How effective are MDP formulations and reward design for different tasks? (3) How do RL and IL compare in performance? (4) Can pre-training on multiple ultrasound simulation models and patients enable zero-shot generalization to unseen ultrasound noise and patients?

Metrics. We quantitatively evaluated ultrasound simulation quality using the learned Perceptual Image Patch Similarity (LPIPS), Structural Similarity Index Measure (SSIM), and Peak Signal-to-Noise Ratio (PSNR) on a testing dataset. We evaluate task performance using environment-specific metrics: **Navigation:** Final 2D position error (projected onto the frontal plane of the patient) and rotation error (around the frontal axis); **Reconstruction:** Coverage ratio (reconstructed vs. total upper surface points), total rotation angle (pitch and yaw), and trajectory length; **Surgery:** Insertion error (position error along the z -axis of $\{G\}$), side error (position error perpendicular to the z -axis

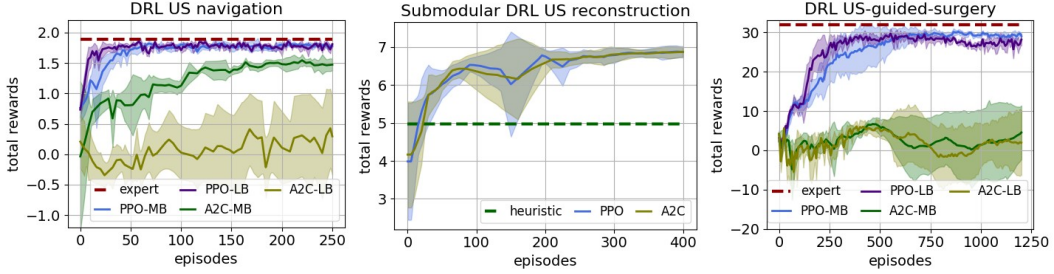


Figure 5: **Learning curves of reinforcement learning agents for all tasks.** The shaded region represents the 1-sigma confidence interval across training runs with five different random seeds. Our modeling allows stable training of PPO agents, which can achieve close performance to expert policies and better performance than A2C agents for *navigation* and *surgery* tasks. For *reconstruction*, both submodular PPO and A2C agents surpass the heuristic trajectory during the learning process.

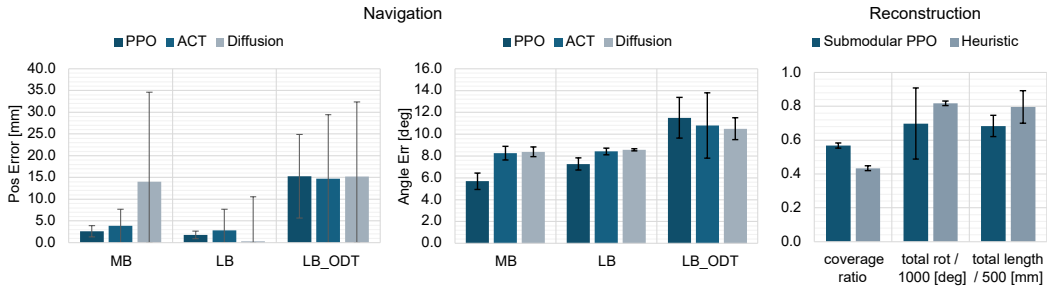


Figure 6: **Performance for navigation and reconstruction.** Results are averaged over 100 trials, and error bars denote the standard deviation. The gaps between LB_ODT and LB are not significant, which demonstrates the potential of sim-to-real transfer over the ultrasound imaging domain. For reconstruction, the submodular PPO policy surpasses the performance of the heuristic policy.

of $\{G\}$), *rotation error* (angle between final drill direction and z -axis of $\{G\}$) and *safe ratio* (the proportion of trajectory states within the safe region).

Experiment setup. We train both PPO and A2C agents for all environments. We also train modified SafeRPlan agents (PPO + safety filter) for the *surgery* task. For the *navigation* and *surgery* tasks, we evaluate the PPO agents on the same type of simulation used during training, corresponding to the ‘MB’ and ‘LB’ groups in Fig. 6 and In-Domain Test (IDT) columns in Tab. 1. To evaluate generalization to varying ultrasound noise conditions, we first train five ultrasound simulation networks with the same data set and different random seeds. We then train agents with 4 of these networks and test them with the 5th network, denoted as Out-of-Domain Test (ODT) columns of ‘LB’ rows in Tab. 1 and ‘LB_ODT’ in Fig. 6. For the *surgery* task, we also tested generalization across patients by training PPO and PPO + safety filter on 5 patients and evaluating on a held-out sixth patient, corresponding to the ODT columns of the ‘MB’ group in Tab. 1. For the reconstruction task, PPO policies were directly evaluated on the same patient and noise distribution.

5.1 Environment Validation

Q1: How realistic and efficient is the ultrasound simulation? Fig. 4 presents a qualitative evaluation of the ultrasound images generated by our pix2pix network. Fig. 4 (left) shows that our network can simulate realistic images during testing. Fig. 4 (right) provides examples of both model-based (MB) and learning-based (LB) ultrasound simulations. Our LB approach maintains high visual quality despite the domain gap between the input CT slices and the training CT data. For quantitative metrics, we achieve LPIPS loss of 0.2415, SSIM score of 0.3940, and PSNR score of 15.96, which is close to the performance of similar works reported in [8]. On an RTX 3090 Ti, the parallel rendering of ultrasound images with size 200×150 of 100 environments takes 0.0089 and

Table 1: Performance of different approaches on the *surgery* task. SF abbreviates safety filter. All values are averaged over 100 trials. The comparable performance between ODT and IDT for LB demonstrates the potential of existing approaches to generalize across the US imaging models.

US sim	Algos	side err ↓[mm]		insert err ↓[mm]		rot err ↓[deg]		safe ratio ↓[%]	
		IDT	ODT	IDT	ODT	IDT	ODT	IDT	ODT
MB	PPO	2.32	5.66	16.0	20.5	5.11	4.54	99.9	88.3
	PPO + SF	2.17	8.94	13.9	27.3	5.36	4.55	100.0	89.8
	ACT	5.38	18.4	2.92	14.5	0.62	5.98	65.9	65.3
LB	PPO	5.42	6.41	12.3	26.9	3.7	3.76	93.1	93.1
	PPO + SF	5.07	4.56	11.9	27.2	3.93	3.59	95.3	96.0
	ACT	5.34	6.26	1.62	1.72	1.01	1.81	86.0	80.3

0.1107 seconds for MB and LB approaches, respectively. This enables training high-performing PPO agents within approximately 2 hours for MB simulations and 10 hours for LB simulations.

Q2: How effective are the MDP formulations and reward design for different tasks?

Fig. 5 shows the training curves for all 3 environments with PPO and A2C. For *navigation* and *surgery* tasks, PPO can achieve close performance to the expert policy (red, based on full states) and better performance than A2C. For reconstruction, both PPO and A2C policies outperform the heuristic trajectory adopted by existing works [24]. As is also demonstrated by Fig. 6 (middle), the learned trajectory exhibits a higher coverage rate (reconstructed points divided by total points) with lower total rotation angles and path length than the heuristic policy. An example learned trajectory with a circular shape is shown in Fig. 7 (left), which is intuitively more efficient than the heuristic trajectory (right) composed mainly of vertical and horizontal segments.

5.2 Comparison study

Q3: How do RL algorithms compare with IL algorithms in different tasks?

Fig. 6 (left) and (middle) show the comparison between PPO, ACT and DP in the *navigation* task. PPO has lower position tracking variance compared to IL approaches. PPO achieves better rotation tracking accuracy. Comparison between PPO, PPO with safety filter and ACT in the *surgery* task is shown in Table. 1. In general, PPO and PPO with safety filter are more safety-aware (higher safety ratio) than ACT. They also achieves lower side position error, which can be due to the larger weight on tracking reward in the drilling region. On the contrary, ACT generally has lower safe ratios but higher tracking accuracy along the insertion direction. Fig. 8 also demonstrates that PPO trajectories are more ‘conservative’ by being concentrated around the goal direction and keeping a margin from the goal position.

Q4: Can pretraining on multiple ultrasound simulation models and patients enable zero-shot generalization to unseen ultrasound noise and patients?

The generalization performance of PPO, ACT and Diffusion policy over observation domain gaps in the *navigation* task is demonstrated in Fig. 6 (left) and (middle), ‘LB_ODT’ groups. The results show that all approaches achieve position errors of less than 16[mm] and

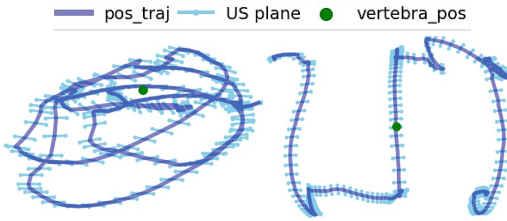


Figure 7: Learned and heuristic trajectories for the Reconstruction task. (left) The learned trajectory exhibits a circular pattern around the target vertebra; (right) the fixed heuristic trajectory.

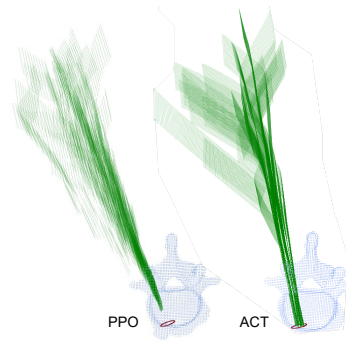


Figure 8: Example trajectories for the surgery task. The example trajectories, target vertebra and the goal position are colored green, blue, and red, respectively. PPO trajectories have less variance and stop at a certain distance from the goal, while ACT policies are less conservative and smoother.

rotation errors less than 12[deg], which is still acceptable for *navigation*. For the *surgery* task, the generalization results ('ODT' columns of 'LB' group) in general has a similar level of performance, with slightly higher *insertion error* and lower safe ratio, as is shown in Tab. 1. This shows the potential of training existing approaches with multiple ultrasound simulation networks to address the sim-to-real gap between images. Regarding testing on a new patient (ODT columns of MB in Tab. 1), both the *safe ratio* and the *side error* have a large gap to the IDT columns. This result shows that generalization across different patients is still challenging, especially with a limited diversity of patient models.

6 Conclusion

We introduce SonoGym, a scalable simulation platform designed for complex robotic ultrasound tasks, offering fast physics-based and realistic learning-based image generation. The platform includes MDP models and expert datasets for ultrasound-guided navigation, bone reconstruction, and spinal surgery, enabling effective training of reinforcement learning and imitation learning agents. Our results highlight the potential of these approaches for sim-to-real generalization over the imaging domain gap. We also identify challenges in generalization over inter-patient variability when relying on limited patient data.

Limitations and future work Several limitations exist for our approach. We generated high-quality ultrasound images using a GAN-based approach; however, the current model does not incorporate physics-based consistency between consecutive frames. Additionally, the patient models—comprising 3D label maps and CT scans—remain static and do not account for soft tissue deformation. The results were obtained from a limited number of patient samples and have not yet been scaled to represent a broader population. Future research directions include improving ultrasound simulation quality and noise diversity, modeling soft tissue deformation, scaling to larger patient populations, improving generalization over different patients, and validation with real robotic ultrasound systems in clinical settings.

References

- [1] Ilge Akkaya, Marcin Andrychowicz, Maciek Chociej, Mateusz Litwin, Bob McGrew, Arthur Petron, Alex Paino, Matthias Plappert, Glenn Powell, Raphael Ribas, et al. Solving rubik’s cube with a robot hand. *arXiv preprint arXiv:1910.07113*, 2019.
- [2] Ahmed Z Alsinan, Charles Rule, Michael Vives, Vishal M Patel, and Ilker Hacihaliloglu. Gan-based realistic bone ultrasound image and label synthesis for improved segmentation. In *Medical Image Computing and Computer Assisted Intervention–MICCAI 2020: 23rd International Conference, Lima, Peru, October 4–8, 2020, Proceedings, Part VI 23*, pages 795–804. Springer, 2020.
- [3] Yunke Ao, Hooman Esfandiari, Fabio Carrillo, Christoph J Laux, Yarden As, Ruixuan Li, Kaat Van Assche, Ayoob Davoodi, Nicola A Cavalcanti, Mazda Farshad, et al. Saferplan: Safe deep reinforcement learning for intraoperative planning of pedicle screw placement. *Medical Image Analysis*, 99:103345, 2025.
- [4] Benny Burger, Sascha Bettinghausen, Matthias Radle, and Jürgen Hesser. Real-time gpu-based ultrasound simulation using deformable mesh models. *IEEE transactions on medical imaging*, 32(3):609–618, 2012.
- [5] Tingxiu Chen, Yilei Shi, Zixuan Zheng, Bingcong Yan, Jingliang Hu, Xiao Xiang Zhu, and Lichao Mou. Ultrasound image-to-video synthesis via latent dynamic diffusion models. In *International Conference on Medical Image Computing and Computer-Assisted Intervention*, pages 764–774. Springer, 2024.
- [6] Cheng Chi, Zhenjia Xu, Siyuan Feng, Eric Cousineau, Yilun Du, Benjamin Burchfiel, Russ Tedrake, and Shuran Song. Diffusion policy: Visuomotor policy learning via action diffusion. *The International Journal of Robotics Research*, page 02783649241273668, 2023.
- [7] Erwin Coumans and Yunfei Bai. Pybullet, a python module for physics simulation for games, robotics and machine learning. <http://pybullet.org>, 2016–2019.

- [8] Marina Domínguez, Yordanka Velikova, Nassir Navab, and Mohammad Farid Azampour. Diffusion as sound propagation: Physics-inspired model for ultrasound image generation. In *International Conference on Medical Image Computing and Computer-Assisted Intervention*, pages 613–623. Springer, 2024.
- [9] Felix Duelmer, Mohammad Farid Azampour, and Nassir Navab. Ultraray: Full-path ray tracing for enhancing realism in ultrasound simulation. *arXiv preprint arXiv:2501.05828*, 2025.
- [10] François Faure, Christian Duriez, Hervé Delingette, Jérémie Allard, Benjamin Gilles, Stéphanie Marchesseau, Hugo Talbot, Hadrien Courtecuisse, Guillaume Bousquet, Igor Peterlik, et al. Sofa: A multi-model framework for interactive physical simulation. *Soft tissue biomechanical modeling for computer assisted surgery*, pages 283–321, 2012.
- [11] Ian J Goodfellow, Jean Pouget-Abadie, Mehdi Mirza, Bing Xu, David Warde-Farley, Sherjil Ozair, Aaron Courville, and Yoshua Bengio. Generative adversarial nets. *Advances in neural information processing systems*, 27, 2014.
- [12] Hannes Hase, Mohammad Farid Azampour, Maria Tirindelli, Magdalini Paschali, Walter Simson, Emad Fatemizadeh, and Nassir Navab. Ultrasound-guided robotic navigation with deep reinforcement learning. In *2020 IEEE/RSJ International Conference on Intelligent Robots and Systems (IROS)*, pages 5534–5541. IEEE, 2020.
- [13] Jonathan Ho, Ajay Jain, and Pieter Abbeel. Denoising diffusion probabilistic models. *Advances in neural information processing systems*, 33:6840–6851, 2020.
- [14] Jemin Hwangbo, Joonho Lee, Alexey Dosovitskiy, Dario Bellicoso, Vassilios Tsounis, Vladlen Koltun, and Marco Hutter. Learning agile and dynamic motor skills for legged robots. *Science Robotics*, 4(26):eaau5872, 2019.
- [15] Phillip Isola, Jun-Yan Zhu, Tinghui Zhou, and Alexei A Efros. Image-to-image translation with conditional adversarial networks. In *Proceedings of the IEEE conference on computer vision and pattern recognition*, pages 1125–1134, 2017.
- [16] Zahra Izadifar, Paul Babyn, and Dean Chapman. Mechanical and biological effects of ultrasound: a review of present knowledge. *Ultrasound in medicine & biology*, 43(6):1085–1104, 2017.
- [17] Zhongliang Jiang, Septimiu E Salcudean, and Nassir Navab. Robotic ultrasound imaging: State-of-the-art and future perspectives. *Medical image analysis*, 89:102878, 2023.
- [18] Dmitry Kalashnikov, Alex Irpan, Peter Pastor, Julian Ibarz, Alexander Herzog, Eric Jang, Deirdre Quillen, Ethan Holly, Mrinal Kalakrishnan, Vincent Vanhoucke, et al. Scalable deep reinforcement learning for vision-based robotic manipulation. In *Conference on robot learning*, pages 651–673. PMLR, 2018.
- [19] Sofoklis Kataklis, Nikolaos Barotsis, Alexandros Kakotaritis, Panagiotis Tsiganos, George Economou, Elias Panagiotopoulos, and George Panayiotakis. Generation of musculoskeletal ultrasound images with diffusion models. *BioMedInformatics*, 3(2):405–421, 2023.
- [20] Peter Kazanzides, Zihan Chen, Anton Deguet, Gregory S Fischer, Russell H Taylor, and Simon P DiMaio. An open-source research kit for the da vinci® surgical system. In *2014 IEEE international conference on robotics and automation (ICRA)*, pages 6434–6439. IEEE, 2014.
- [21] Oliver Kutter, Ramtin Shams, and Nassir Navab. Visualization and gpu-accelerated simulation of medical ultrasound from ct images. *Computer methods and programs in biomedicine*, 94(3):250–266, 2009.
- [22] Ang Li, Jiayi Han, Yongjian Zhao, Keyu Li, and Li Liu. Realistic ultrasound synthesis based on diagnostic ct to facilitate ultrasound-guided robotic spine surgery. *IEEE Transactions on Medical Robotics and Bionics*, 5(4):879–889, 2023.
- [23] Keyu Li, Jian Wang, Yangxin Xu, Hao Qin, Dongsheng Liu, Li Liu, and Max Q-H Meng. Autonomous navigation of an ultrasound probe towards standard scan planes with deep reinforcement learning. In *2021 IEEE International Conference on Robotics and Automation (ICRA)*, pages 8302–8308. IEEE, 2021.

- [24] Ruixuan Li, Ayoob Davoodi, Yuyu Cai, Kenan Niu, Gianni Borghesan, Nicola Cavalcanti, Aidana Massalimova, Fabio Carrillo, Christoph J Laux, Mazda Farshad, et al. Robot-assisted ultrasound reconstruction for spine surgery: from bench-top to pre-clinical study. *International journal of computer assisted radiology and surgery*, 18(9):1613–1623, 2023.
- [25] Ruixuan Li, Ayoob Davoodi, Maikel Timmermans, Kaat Van Assche, Orçun Taylan, Lennart Scheys, Matthias Tummers, Gianni Borghesan, and Emmanuel Vander Poorten. Ultrasound-based robot-assisted drilling for minimally invasive pedicle screw placement. *IEEE Transactions on Medical Robotics and Bionics*, 6(3):818–828, 2024.
- [26] Jiamin Liang, Xin Yang, Yuhao Huang, Haoming Li, Shuangchi He, Xindi Hu, Zejian Chen, Wufeng Xue, Jun Cheng, and Dong Ni. Sketch guided and progressive growing gan for realistic and editable ultrasound image synthesis. *Medical image analysis*, 79:102461, 2022.
- [27] Yonghao Long, Wang Wei, Tao Huang, Yuehao Wang, and Qi Dou. Human-in-the-loop embodied intelligence with interactive simulation environment for surgical robot learning. *IEEE Robotics and Automation Letters*, 8(8):4441–4448, 2023.
- [28] Viktor Makoviychuk, Lukasz Wawrzyniak, Yunrong Guo, Michelle Lu, Kier Storey, Miles Macklin, David Hoeller, Nikita Rudin, Arthur Allshire, Ankur Handa, et al. Isaac gym: High performance gpu-based physics simulation for robot learning. *arXiv preprint arXiv:2108.10470*, 2021.
- [29] Oliver Mattausch, Maxim Makhinya, and Orcun Goksel. Realistic ultrasound simulation of complex surface models using interactive monte-carlo path tracing. In *Computer Graphics Forum*, volume 37, pages 202–213. Wiley Online Library, 2018.
- [30] Takahiro Miki, Joonho Lee, Jemin Hwangbo, Lorenz Wellhausen, Vladlen Koltun, and Marco Hutter. Learning robust perceptive locomotion for quadrupedal robots in the wild. *Science robotics*, 7(62):eabk2822, 2022.
- [31] Mayank Mittal, Calvin Yu, Qinx Yu, Jingzhou Liu, Nikita Rudin, David Hoeller, Jia Lin Yuan, Ritvik Singh, Yunrong Guo, Hammad Mazhar, Ajay Mandlekar, Buck Babich, Gavriel State, Marco Hutter, and Animesh Garg. Orbit: A unified simulation framework for interactive robot learning environments. *IEEE Robotics and Automation Letters*, 8(6):3740–3747, 2023.
- [32] Volodymyr Mnih, Adria Puigdomenech Badia, Mehdi Mirza, Alex Graves, Timothy Lillicrap, Tim Harley, David Silver, and Koray Kavukcuoglu. Asynchronous methods for deep reinforcement learning. In *International conference on machine learning*, pages 1928–1937. PMLR, 2016.
- [33] Masoud Moghani, Nigel Nelson, Mohamed Ghanem, Andres Diaz-Pinto, Kush Hari, Mahdi Azizian, Ken Goldberg, Sean Huver, and Animesh Garg. Sufia-bc: Generating high quality demonstration data for visuomotor policy learning in surgical subtasks. *arXiv preprint arXiv:2504.14857*, 2025.
- [34] Guochen Ning, Xinran Zhang, and Hongen Liao. Autonomic robotic ultrasound imaging system based on reinforcement learning. *IEEE transactions on biomedical engineering*, 68(9):2787–2797, 2021.
- [35] Prashant Pandey, Pierre Guy, Antony J Hodgson, and Rafeef Abugharbieh. Fast and automatic bone segmentation and registration of 3d ultrasound to ct for the full pelvic anatomy: a comparative study. *International journal of computer assisted radiology and surgery*, 13:1515–1524, 2018.
- [36] Matteo Pavone, Barbara Seeliger, Elena Teodorico, Marta Goglia, Cristina Taliento, Nicolò Bizzarri, Lise Lecointre, Cherif Akladios, Antonello Forgione, Giovanni Scambia, et al. Ultrasound-guided robotic surgical procedures: a systematic review. *Surgical endoscopy*, 38(5):2359–2370, 2024.
- [37] Manish Prajapat, Mojmir Mutny, Melanie Zeilinger, and Andreas Krause. Submodular reinforcement learning. In *The Twelfth International Conference on Learning Representations*, 2024.

- [38] Mehrdad Salehi, Seyed-Ahmad Ahmadi, Raphael Prevost, Nassir Navab, and Wolfgang Wein. Patient-specific 3d ultrasound simulation based on convolutional ray-tracing and appearance optimization. In *Medical Image Computing and Computer-Assisted Intervention–MICCAI 2015: 18th International Conference, Munich, Germany, October 5–9, 2015, Proceedings, Part II 18*, pages 510–518. Springer, 2015.
- [39] Paul Maria Scheikl, Balázs Gyenes, Rayan Younis, Christoph Haas, Gerhard Neumann, Martin Wagner, and Franziska Mathis-Ullrich. Lapgym—an open source framework for reinforcement learning in robot-assisted laparoscopic surgery. *Journal of Machine Learning Research*, 24(368):1–42, 2023.
- [40] Samuel Schmidgall, Axel Krieger, and Jason Eshraghian. Surgical gym: A high-performance gpu-based platform for reinforcement learning with surgical robots. *arXiv preprint arXiv:2310.04676*, 2023.
- [41] John Schulman, Filip Wolski, Prafulla Dhariwal, Alec Radford, and Oleg Klimov. Proximal policy optimization algorithms, 2017.
- [42] Antonio Serrano-Muñoz, Dimitrios Chrysostomou, Simon Bøgh, and Nestor Arana-Arexolaleiba. skrl: Modular and flexible library for reinforcement learning. *Journal of Machine Learning Research*, 24(254):1–9, 2023.
- [43] Ramtin Shams, Richard Hartley, and Nassir Navab. Real-time simulation of medical ultrasound from ct images. In *Medical Image Computing and Computer-Assisted Intervention–MICCAI 2008: 11th International Conference, New York, NY, USA, September 6–10, 2008, Proceedings, Part II 11*, pages 734–741. Springer, 2008.
- [44] Kihyuk Sohn, Honglak Lee, and Xinchen Yan. Learning structured output representation using deep conditional generative models. *Advances in neural information processing systems*, 28, 2015.
- [45] Yuhan Song and Nak Young Chong. S-cyclegan: Semantic segmentation enhanced ct-ultrasound image-to-image translation for robotic ultrasonography. In *2024 IEEE International Conference on Cyborg and Bionic Systems (CBS)*, pages 115–120. IEEE, 2024.
- [46] David Stojanovski, Uxio Hermida, Pablo Lamata, Arian Beqiri, and Alberto Gomez. Echo from noise: synthetic ultrasound image generation using diffusion models for real image segmentation. In *International Workshop on Advances in Simplifying Medical Ultrasound*, pages 34–43. Springer, 2023.
- [47] Jie Tan, Tingnan Zhang, Erwin Coumans, Atil Iscen, Yunfei Bai, Danijar Hafner, Steven Bohez, and Vincent Vanhoucke. Sim-to-real: Learning agile locomotion for quadruped robots. *arXiv preprint arXiv:1804.10332*, 2018.
- [48] Emanuel Todorov, Tom Erez, and Yuval Tassa. Mujoco: A physics engine for model-based control. In *2012 IEEE/RSJ international conference on intelligent robots and systems*, pages 5026–5033. IEEE, 2012.
- [49] Kaat Van Assche, Ruixuan Li, Ayoob Davoodi, Matthias Tummers, Mouloud Ourak, Gianni Borghesan, Nicola Cavalcanti, Philipp Fünstahl, and Emmanuel Vander Poorten. Robotic path re-planning for us reconstruction of the spine. *IEEE Transactions on Medical Robotics and Bionics*, 2025.
- [50] Ashish Vaswani, Noam Shazeer, Niki Parmar, Jakob Uszkoreit, Llion Jones, Aidan N Gomez, Łukasz Kaiser, and Illia Polosukhin. Attention is all you need. *Advances in neural information processing systems*, 30, 2017.
- [51] Maria Victorova, Michael Ka-Shing Lee, David Navarro-Alarcon, and Yongping Zheng. Follow the curve: Robotic ultrasound navigation with learning-based localization of spinous processes for scoliosis assessment. *IEEE access*, 10:40216–40229, 2022.

- [52] Jakob Wasserthal, Hanns-Christian Breit, Manfred T Meyer, Maurice Pradella, Daniel Hinck, Alexander W Sauter, Tobias Heye, Daniel T Boll, Joshy Cyriac, Shan Yang, et al. Totalsegmentator: robust segmentation of 104 anatomic structures in ct images. *Radiology: Artificial Intelligence*, 5(5):e230024, 2023.
- [53] Luohong Wu, Nicola A Cavalcanti, Matthias Seibold, Giuseppe Loggia, Lisa Reissner, Jonas Hein, Silvan Beeler, Arnd Viehöfer, Stephan Wirth, Lilian Calvet, et al. Ultrabones100k: A reliable automated labeling method and large-scale dataset for ultrasound-based bone surface extraction. *arXiv preprint arXiv:2502.03783*, 2025.
- [54] Jiaqi Xu, Bin Li, Bo Lu, Yun-Hui Liu, Qi Dou, and Pheng-Ann Heng. Surrol: An open-source reinforcement learning centered and dvrk compatible platform for surgical robot learning. In *2021 IEEE/RSJ International Conference on Intelligent Robots and Systems (IROS)*, pages 1821–1828. IEEE, 2021.
- [55] Qinxi Yu, Masoud Moghani, Karthik Dharmarajan, Vincent Schorp, William Chung-Ho Panitch, Jingzhou Liu, Kush Hari, Huang Huang, Mayank Mittal, Ken Goldberg, et al. Orbit-surgical: An open-simulation framework for learning surgical augmented dexterity. In *2024 IEEE International Conference on Robotics and Automation (ICRA)*, pages 15509–15516. IEEE, 2024.
- [56] Tony Z Zhao, Vikash Kumar, Sergey Levine, and Chelsea Finn. Learning fine-grained bimanual manipulation with low-cost hardware. *arXiv preprint arXiv:2304.13705*, 2023.
- [57] Weiye Zhao, Rui Chen, Yifan Sun, Tianhao Wei, and Changliu Liu. State-wise constrained policy optimization, 2024.
- [58] Jun-Yan Zhu, Taesung Park, Phillip Isola, and Alexei A Efros. Unpaired image-to-image translation using cycle-consistent adversarial networks. In *Proceedings of the IEEE international conference on computer vision*, pages 2223–2232, 2017.

A Dataset access

Below are the links to our project website, source code, simulation assets, and expert dataset.

Project website: <https://sonogym.github.io/>.

Code: <https://github.com/SonoGym/SonoGym>.

Simulation assets: https://huggingface.co/datasets/yunkao/SonoGym_assets_models.

Expert dataset: https://huggingface.co/datasets/yunkao/SonoGym_lerobot_dataset

B Simulation details

B.1 Assets

We provide both the KUKA Med14 and Franka Emika Panda robot arms for ultrasound probe manipulation. To generate joint-space commands for robot control, we employ differential inverse kinematics controllers from IsaacLab. For the patient dataset, we process 3D CT images and corresponding label maps from 10 subjects in the TotalSegmentator dataset, capturing anatomical variability as illustrated in Fig. 9. Each patient’s torso is converted into an STL mesh to enable physical interaction with the robot arms and patient beds in IsaacLab simulation environments. These torso models are treated as rigid bodies and are spatially aligned with their respective CT volumes and label maps. For each patient, we define the surgical target pose at the L4 vertebra using our in-house planning software, which incorporates clinical requirements for pedicle screw insertion trajectories.

B.2 Ultrasound simulation

Model-based approach We follow the ray-tracing-based model introduced in [38] for ultrasound simulation. The ultrasound image $I \in \mathbb{R}^{H \times W}$ consists of a reflection component $R \in \mathbb{R}^{H \times W}$ and a backscattered component $B \in \mathbb{R}^{H \times W}$: $I = R + B$. For each 2D pixel position $u := (x, y)$, where $x \in [0, W]$ and $y \in [0, H]$, the reflection term R is computed as:

$$R(u) = |E(u) \cdot \cos \Theta(u) \cdot \frac{Z(x, y + \delta y) - Z(x, y)}{Z(x, y + \delta y) + Z(x, y)}| \cdot P(u) \otimes G(u)$$

where $E(u)$ is the remaining energy at u , $\Theta(u)$ is the incidence angle of the ray (along the $+y$ direction) at the medium boundary surface, $Z(x, y)$ denotes the acoustic impedance of the tissue, δy is the vertical image resolution, $P(u)$ is the point spread function (PSF), $G(u)$ is the indicator function for surface boundaries, and \otimes denotes convolution. The remaining energy $E(u)$ is computed based on the attenuation coefficients α of the tissue at each position:

$$E(u) = E_0 \exp \left(-f \cdot \int_0^y \alpha(x, v), dv \right),$$

where f is the ultrasound frequency and E_0 is the initial energy. The acoustic impedance $Z(u)$ is set proportional to the CT intensity, following [21]. The attenuation map α is determined based on the ultrasound simulation settings from Imfusion Suite [38]². The PSF is modeled with a 2D Gaussian kernel with variances approximately 1% of the image size. G and Θ are obtained from the 2D label slice.

The backscattering term B is computed as:

$$B(u) = E(u) \cdot P(u) \otimes T(u)$$

where $T(u)$ represents the scattering pattern. $T(u)$ is determined using three tissue parameters σ_0 , μ_0 , and μ_1 , along with two Gaussian noise maps N_0 and N_1 :

$$\begin{aligned} \tilde{T}(u) &= N_0(u) \cdot \sigma_0(u) + \mu_0(u) \\ T(u) &= \begin{cases} \tilde{T}(u), & N_1(u) \leq \mu_1(u) \\ 0, & \text{otherwise} \end{cases} \end{aligned}$$

²<https://www.imfusion.com/>

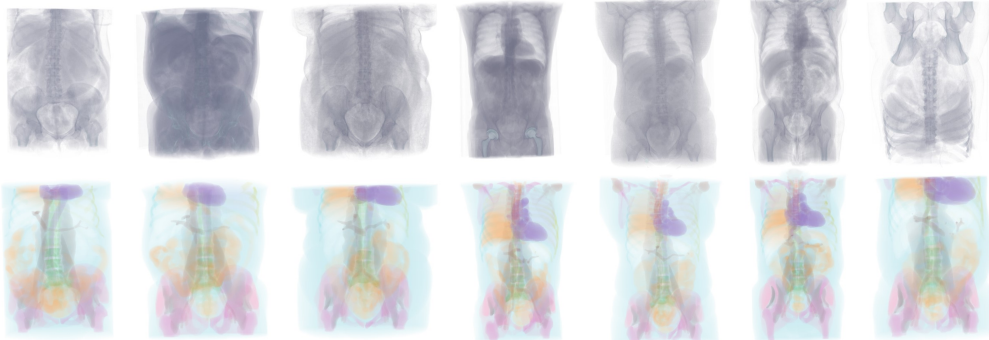


Figure 9: **Patient anatomy data from TotalSegmentator dataset.** We provide ultrasound simulation based on diverse real patient models, including CT volume and segmentation.

The noise maps N_0 and N_1 are sampled over the 3D space at initialization and remain fixed throughout the online simulation. σ_0 , μ_0 , and μ_1 of each tissue are determined based on settings in Imfusion. To capture spatial scattering variations at larger scales, we additionally incorporate multi-scale versions of N_0 and N_1 , following the approach introduced in [29].

Learning-based approach We follow the setup described in [53] to collect a dataset of paired CT-US images from seven ex-vivo spine specimens. Optical markers are attached to the sacrum of each specimen, and additional K-wires (2.5 mm in diameter, 150 mm in length; DePuy Synthes, USA) are used to stabilize each vertebra, avoiding bone movement during data acquisition. CT scans were acquired for each specimen with an image resolution of 512×512 pixels, an in-plane pixel spacing of $0.839 \text{ mm} \times 0.839 \text{ mm}$, and a slice thickness of 0.6 mm (NAEOTOM Alpha, Siemens, Germany). For ultrasound imaging, we used the Aixplorer Ultimate system (SuperSonic Imagine, Aix-en-Provence, France) equipped with an SL18-5 linear probe (SuperSonic Imagine, Aix-en-Provence, France). An optical marker was attached to the ultrasound probe for pose tracking using an optical tracking system (FusionTrack 500, Atracsys, Switzerland). We follow the calibration pipeline in [53] to calibrate the ultrasound probe. Based on tracking data from both the spine specimen and the ultrasound probe, we register the CT and US volumes, enabling the generation of paired CT-US images.

Our pix2pix network adopts the deep U-Net architecture illustrated in Fig. 11. The model is trained using a combination of L1 loss and GAN loss, with respective weights of 1 and 0.01. In total, we train five separate networks for 15–25 epochs on our training dataset. To improve generalization to unseen CT resolutions (such as those encountered in our simulation data), we apply data augmentation via random downsampling and upsampling.

C Environments details

C.1 Task 1: Ultrasound navigation

Environment settings The initial 2D pose of the ultrasound probe is randomized within a $130 \times 130 [\text{mm}^2]$ region on the frontal plane of the patient, like the region shown in Fig. 10. The orientation of the probe is initialized with a rotation between 1.5 and $3.5 [\text{rad}]$ from the transverse plane. We set the ultrasound image size to 200×150 pixels, with a spatial resolution of $0.5 [\text{mm}]$ per pixel. For the reward function, we assign a weight of $w_1 = 0.045$ to balance the position error (in $[\text{mm}]$) and rotation error (in $[\text{rad}]$).

Agents The network architecture used for the PPO and A2C agents is shown in Fig. 12, comprising 4 convolutional layers followed by 3 fully connected layers. The agents are provided by the SKRL [42] library, which supports the



Figure 10: **Top-down view of region of manipulating the probe.**

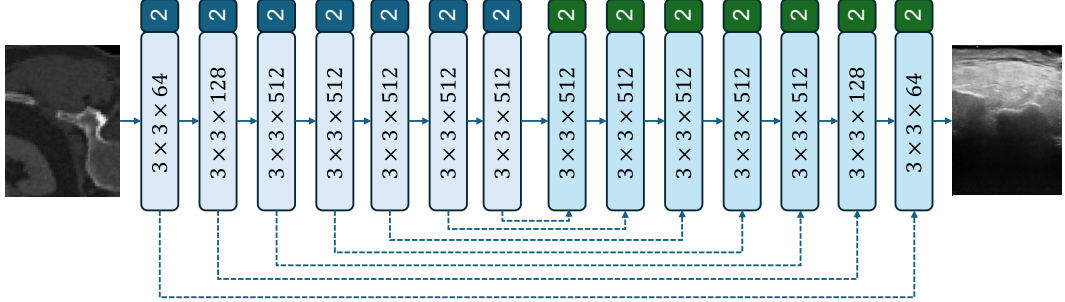


Figure 11: **U-Net architecture used for learning-based ultrasound simulation.** Dashed lines indicate residual connections within the U-Net. Convolutional (blue) and transposed convolutional (cyan) layers are annotated with (kernel size) \times (kernel size) \times (number of channels). The values in the blue and green blocks denote the stride used for downsampling and upsampling, respectively.

KLAdaptiveLR scheduler for the PPO agent. The hyperparameters used for training are listed in Tab.2 and Tab.3. Training is performed with 128 parallel environments, each with an episode length of 300 steps. For imitation learning, we construct expert datasets using our expert policy from three settings:

- model-based ultrasound simulation with a single patient (MB),
- learning-based simulation with a single patient (LB),
- learning-based simulation using four distinct simulation networks (LB 4 net).

The number of episodes in each dataset is 2052, 1869, and 954, respectively, as summarized in Tab. 4.

C.2 Task 2: Bone surface reconstruction

Environment settings The observation volume has a shape of $40 \times 40 \times 40$ voxels with a voxel resolution of 3 [mm]. At each time step, a new 2D ultrasound image is received from the probe, and we assume that a segmentation of the bone surface is available from this image. This segmentation is simulated from the ground truth bone surface by independently applying a missing probability of 20% to each ground truth surface point. The resulting 2D segmentation map is then used to update the 3D surface reconstruction based on the current pose of the ultrasound probe. The initial 2D position of the ultrasound probe in the patient’s frontal plane is randomized within a 30×30 [mm 2] region centered around the target vertebra position. For reward design, we use weights $w_2 = 0.01$ and $w_3 = 1$ to balance the amount of surface coverage with the total trajectory length and rotation angle.

Agents The network architecture of the PPO and A2C agents is illustrated in Fig.12, which contains 3 convolutional layers and 3 fully-connected layers. The hyperparameters are shown in Tab. 2 and Tab. 3. The agents are trained with 128 parallel environments with episode length 300.

Table 2: Hyperparameters of PPO agent.

Hyperparameters	navigation	reconstruction	surgery
rollouts	32	32	16
learning_epochs	5	3	3
mini_batches	32	4	32
discount_factor	0.99	0.99	0.99
lambda	0.95	0.95	0.95
learning_rate	0.0001	0.0003	0.0001
learning_rate_scheduler:	KLAdaptiveLR	KLAdaptiveLR	KLAdaptiveLR
kl_threshold:	0.008	0.008	0.008
grad_norm_clip	1	1	1
ratio_clip	0.2	0.2	0.2
value_clip	0.2	0.1	0.1
value_loss_scale	1	1	1

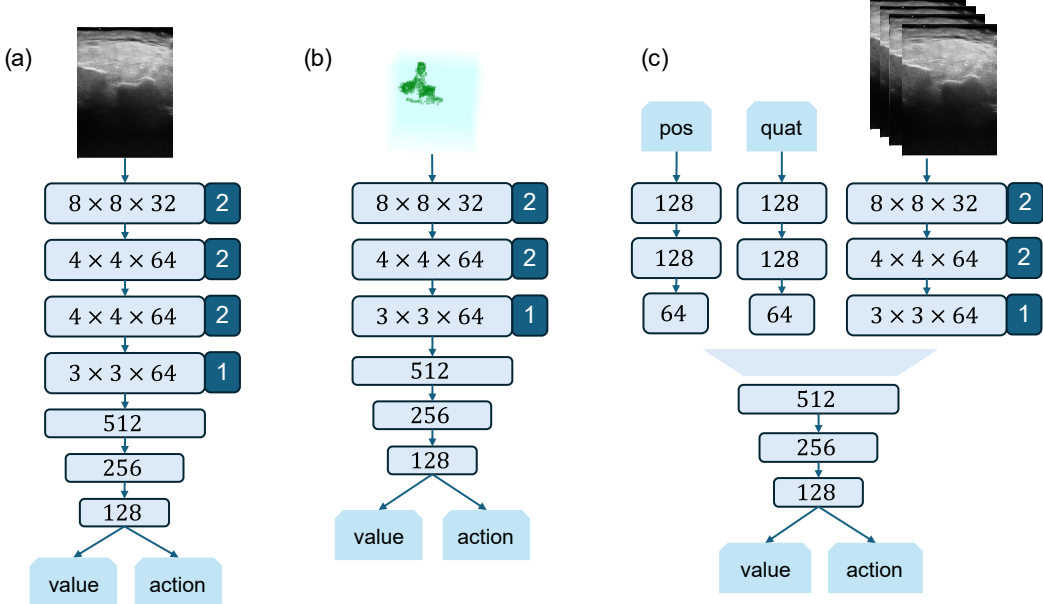


Figure 12: **Network architecture** for (a) *navigation*, (b) *reconstruction* and (c) *surgery*. The convolution layers are represented by (kernel size) \times (kernel size) \times (number of channels). The numbers in the blue block on the right is the numbers of strides.

Table 3: Hyperparameters of A2C agents.

Hyperparameters	<i>navigation</i>	<i>reconstruction</i>	<i>surgery</i>
rollouts	16	64	64
learning_epochs	5	3	1
mini_batches	32	32	4
discount_factor	0.99	0.99	0.99
lambda	0.95	0.95	0.95
learning_rate	0.0001	0.0001	0.0001
grad_norm_clip	1	1	1

Table 4: Number of episodes for expert datasets.

Settings	<i>navigation</i>	<i>surgery</i>
MB	2052	3536
MB 5 patients	-	1476
LB	1869	2052
LB 4 net	954	2692

C.3 Task 3: Ultrasound-guided surgery

Environment settings The size of 3D ultrasound volume for the *surgery* task is $50 \times 37 \times 5$, with resolutions $2 \times 2 \times 10 [\text{mm}^3]$ along height, width, and elevation, respectively. The initial joint angles of the drill robot are randomized within $[-1.5 \pm 0.2, -0.2 \pm 0.1, 0.0 \pm 0.1, -1.3 \pm 0.1, 0.0 \pm 0.1, 1.8 \pm 0.1, 0.0 \pm 0.1]^\top [\text{rad}]$. The starting point of the trajectory on the skin is defined as $p_l = [0, 0, -50] [\text{mm}]$ in the goal frame $\{G\}$. The position of the ultrasound probe above the target vertebra is set above the center of the vertebra with 30 [mm] translation to the ultrasound robot side. This position is further randomized within a range of 5 [mm] along all tangential axes. The reward weights are set as $w_4 = 30$, $w_5 = 5$, and $w_6 = 300$ to encourage the agent to minimize the *side error* during insertion.

Agents The network architecture of the PPO and A2C agents is illustrated in Fig. 12. It consists of three convolutional layers for encoding image features, three fully connected layers for encoding positional information, and three fully connected layers for encoding quaternion representations.

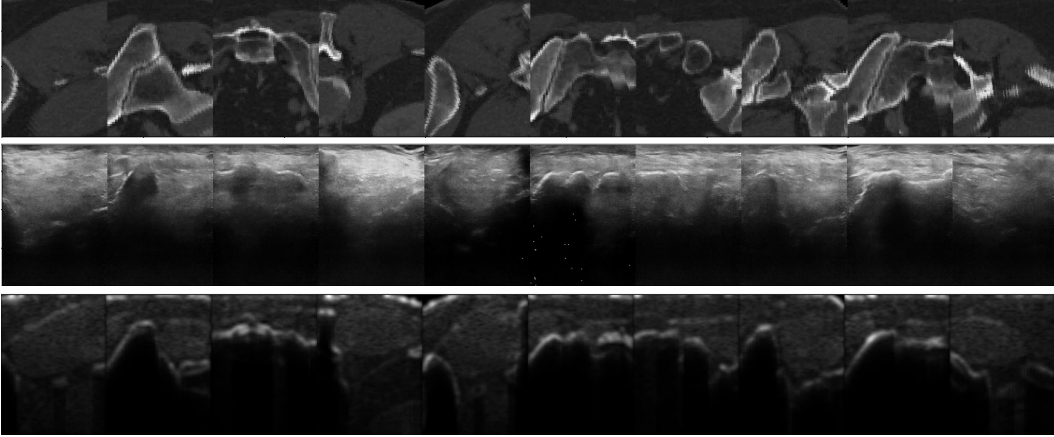


Figure 13: **Additional qualitative results of ultrasound simulation.** The top, middle, and down rows are CT slices, learning-based ultrasound simulation and model-based ultrasound simulation, respectively.

These feature streams are then concatenated and processed by an additional three fully connected layers. The training hyperparameters are summarized in Tab.2 and Tab.3. The agents are trained with 128 parallel environments with episode length of 600 steps. For the expert dataset for imitation learning, we provide datasets collected from four different settings:

- model-based ultrasound simulation from a single patient (MB),
- model-based ultrasound simulation from 5 patients (MB 5 patients),
- learning-based simulation from a single patient (LB),
- learning-based simulation with 4 simulation networks (LB 4 net).

The corresponding numbers of episodes are 3536, 1476, 2052, and 2692, respectively, as shown in Tab. 4. To increase dataset variability, we expand the range of initial robot joint angles as $[-1.6 \pm 0.3, -0.0 \pm 0.25, 0.0 \pm 0.2, -1.3 \pm 0.2, 0.0 \pm 0.2, 1.8 \pm 0.2, 0.0 \pm 0.1]^\top$ [rad], enabling the drill to start from configurations that may fall within unsafe regions.

D Additional results

D.1 Ultrasound simulation

We provide additional examples of learning-based ultrasound simulation for qualitative evaluation. Fig. 13 presents more comparisons between CT slice, model-based and learning-based ultrasound simulations. In CT slices where bone structures exhibit low contrast relative to surrounding tissues, the network occasionally struggles to generate clear bone surfaces and corresponding shadows in the ultrasound images. Although bone surfaces are clearly rendered in many cases, the bone shadows sometimes appear insufficiently dark beneath certain surfaces. We also analyze the variability across different generative networks when given the same CT slice input, as illustrated in Fig. 14. Despite all networks being trained on the identical dataset, different random seeds lead to diverse ultrasound texture patterns. This enables improved image-domain generalization of the agents by randomly sampling from multiple simulation networks during training.

D.2 Reinforcement learning and imitation learning

How effectively do learned and heuristic policies cover the surface? A comparison of reconstructed surfaces between the learned and heuristic policies is shown in Fig. 15. The learned policy demonstrates greater surface coverage, particularly from the back and side views. This improvement may stem from the DRL agents learning to adjust the probe’s pitch, allowing them to capture more points on surface regions where the normals are not oriented vertically.

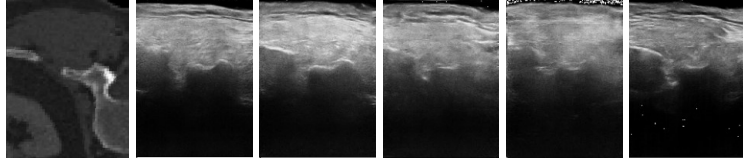


Figure 14: **Variation between ultrasound simulation models.** The input CT slice is shown left, and the other 5 ultrasound images are generated from different models with the same CT input.

Table 5: Side errors, insertion errors and rotation errors achieved by different approaches in the *surgery* task, with standard deviations included (in contrast to Tab. 1).

US sim	Algos	side err ↓[mm]		insert err ↓[mm]		rot err ↓[deg]	
		IDT	ODT	IDT	ODT	IDT	ODT
MB	PPO	2.32 ± 1.3	5.66 ± 18.5	16.0 ± 5.5	20.5 ± 8.0	5.11 ± 1.6	4.54 ± 4.4
	PPO + SF	2.17 ± 1.2	8.94 ± 6.1	13.9 ± 3.3	27.3 ± 5.6	5.36 ± 2.2	4.55 ± 2.5
	ACT	5.38 ± 2.7	18.4 ± 9.8	2.92 ± 1.1	14.5 ± 4.7	0.62 ± 0.8	5.98 ± 2.7
LB	PPO	5.42 ± 4.9	6.41 ± 2.6	12.3 ± 3.2	26.9 ± 4.7	3.7 ± 1.6	3.76 ± 2.5
	PPO + SF	5.07 ± 5.5	4.56 ± 7.0	11.9 ± 7.5	27.2 ± 4.1	3.93 ± 2.5	3.59 ± 1.8
	ACT	5.34 ± 3.0	6.26 ± 2.6	1.62 ± 0.9	1.72 ± 1.4	1.01 ± 1.0	1.81 ± 1.1

How well do agents generalize to a new patient with learning-based ultrasound simulation? As shown in Tab.6, the performance on a previously unseen patient remains significantly lower compared to the results in Tab.5. This highlights the challenge of achieving generalization across anatomical variations when training with a limited number of patient examples.

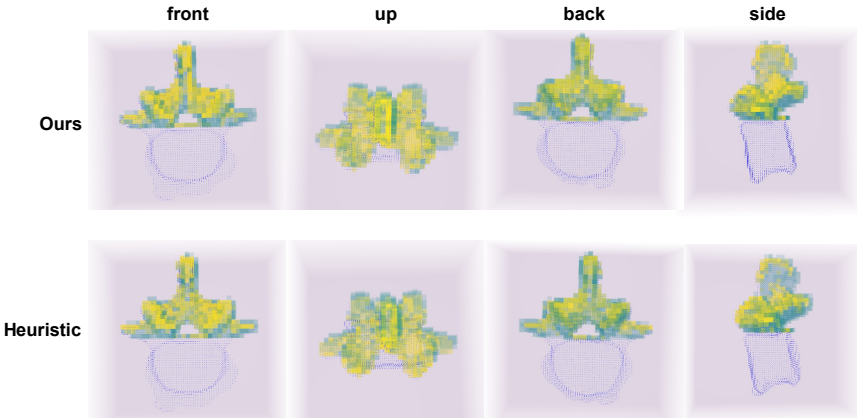


Figure 15: **Reconstructed surfaces.** The reconstructed points and uncovered points on the bone surface are colored yellow and green, respectively. The DRL policy has higher coverage from the back and side views.

What about other agents? We also trained Soft Actor-Critic (SAC) agents for both the *navigation* and *surgery* tasks, but were unable to obtain high-performing policies. We adopted the same network architecture as in our PPO/A2C experiments, but without sharing the encoder between the policy and value networks. Our hyperparameter search covered the following ranges: actor learning rate (0.00001, 0.0001, 0.001), critic learning rate (0.00001, 0.0001, 0.001), gradient steps (1, 8, 32), and batch size (64, 256). We set the replay buffer size to 64,000, taking into account the high memory usage of image observations.

For the *surgery* task, we additionally trained PPO-Lagrangian agents using the following hyperparameter search ranges: learning rates 0.0001 with KLAdaptiveLR scheduler, number of rollouts (16, 32, 64), number of mini-batches (4, 32, 128), number of learning epochs (1, 3, 5), and value loss scale (1.0, 3.0, 10.0). However, none of these configurations resulted in consistently successful policies.

Table 6: Performance of different approaches on a new patient for the *surgery* task with learning-based ultrasound simulation

Algos	side err [mm]	insert err [mm]	rot err [deg]	safe ratio [%]
PPO	27.3 ± 36.4	12.1 ± 8.77	8.28 ± 7.33	52.86
PPO + SF	17.6 ± 54.2	11.2 ± 7.48	8.02 ± 7.12	60.08
ACT	20.7 ± 15.6	15.4 ± 3.92	7.64 ± 2.85	72.06

While Decision Transformer (DP) achieved promising results for the *navigation* task, it failed to perform well on the *surgery* task using the default settings. We experimented with varying the number of historical observation steps (1, 2), action steps (4, 8), planning horizons (8, 16), and learning rates (0.00001, 0.0001), but these adjustments did not lead to significant performance improvements.